Advanced Steel Construction – Vol. 20 No. 2 (2024) 160–168
DOI:10.18057/IJASC.2024.20.2.8
(Special Issue: *11st International Conference on Advances in Steel Structures, ICASS'2023, Kuching, Sarawak, Malaysia*)

EXPERIMENTAL STUDY OF SCISSOR FRAME STRUCTURES WITH FEM VALIDATION OF LOAD IMPACT ON MANUAL LOCKING MECHANISM

Jian Jun Moy and Cher Siang Tan *

Faculty of Civil Engineering, Universiti Teknologi Malaysia, Johor, Malaysia
** (Corresponding author: E-mail: tcsiang@utm.my)*

ABSTRACT

Scissor frame structures (SFS) have attracted significant attention due to their flexibility of deployment and stiffens once fully deployed. These features benefit prefabrication and transportation over traditional frame structures, with potential for modular structure implementation. However, current research often neglects structural analysis, focusing on geometrical and kinematic designs. This oversight, combined with critical load conditions at the locking mechanism linkage, risk underdesigning the SFS and leading to potential structural failure. This study conducted load testing on four SFS specimens with varying cross-sections and heights. Results were discussed based on the measured strain, displacement, and validation with FEM modelling. Analysis shows that despite the flexibility inherent in their pivotal points and multi-plane connections, the SFS exhibits linear behavior under external loads within the elastic range, with symmetrical results akin to single-plane action. Furthermore, three SFS FEM models, developed using SCIA Engineer software, were validated and revealed that loading on the locking mechanism linkage severely impacts structural efficiency. The capacities of the SFS specimens, calculated based on measured critical stress and stiffness, highlight the diverse effects of scissor depth and cross-section on SFS structural behaviour. This paper provides essential experimental data for SFS, assisting engineers in precise structural analysis and assessment.

ARTICLE HISTORY

Received: 8 April 2024
Revised: 5 June 2024
Accepted: 11 June 2024

KEYWORDS

Scissor frame structures;
Locking mechanism and linkage;
Experimental test;
Stress and stiffness;
Fabrication imperfections;
FEM modelling

1. Introduction

Deployable structures are designed to be deployed and retracted along a predetermined deployment path, offering the flexibility to meet specific application requirements while allowing for convenient storage. Extensive research has been conducted on deployable structures, including various types [1]. Scissor structures, also known as scissor frame structures (SFS), are among the most widely used deployable structures in the industry in different fields, which are widely used in aerospace [2], mechanical [3] and civil engineering [4, 5]. The advantage of the SFS over other deployable structures is that it is easier to build and assemble because it only requires a single 1-D member, comparable to a frame structure. Furthermore, unlike other structures, SFS can be constructed to fold into a very compact form, as examined by T.H. Kim [6]. In order to construct an SFS, a pivotal point is introduced on the intermediate length of the members. The behaviour of the SFS can be significantly influenced by the geometry of the scissor members and the location of the pivotal point. The three most commonly used scissors units were translational [7], polar [8], and angulated [9] units. These mechanisms were ingeniously merged to construct numerous SFS that can carry out wide range of functions when implemented in practical applications. According to the literature [10, 11], the integration of deployable structures and modular systems constitutes a significant development in construction technology. These innovative designs are not only easier to fabricate and transport but also possess the ability to expand and withstand substantial loads, ensuring they perform their intended functions effectively. Understanding the load behavior of SFS under real-world conditions remains crucial for maintaining their structural integrity and performance. By addressing these considerations, the construction industry can maximize the utility and efficiency of these advanced systems, enhancing adaptability, cost-effectiveness, and sustainability in modern building practices.

The application of deployable structures includes large-span roof structures [12-14], bridge structures [4, 5], temporary structures [15] and scaffoldings [16]. Previously, Emilio Perez Pinero constructed a deployable structure with a movable theatre utilising the translational unit [17]. Felix Escrig's proposal to use an SFS as a roof cover for a swimming pool in Seville [18] has proven successful, with the structure still standing today. These large-scaled applications have demonstrated the use of SFS and their benefits in construction. However, despite the success of these constructions, current research trend on SFS often revolves around trial-an-error geometrical form-finding method [19] and analytical methods [7, 8] to design the form without considering the structural integrity under various load conditions. In an article published by K. K. Vu et al. [20], the authors acknowledge the issue of neglecting structural stability during the kinematic and geometrical form-finding design of the SFS. Their study proposes to perform an exhaustive approach to generate alternative forms of Deployable Tension-Struct Structures (DTSS) incorporating kinematic and stability checks during the iterations. However, despite these advancements, the structural performance of SFS remains underexplored compared to their kinematic and geometrical design. This highlights the need for further research focusing on the load-bearing capabilities and real-world performance of SFS.

Without boundary conditions, an SFS is essentially a mechanism due to its inherent mobility and cannot carry any external load. However, by introducing additional bars or supports to limit its deployed height or length, the mechanism becomes static and capable of resisting external loads [21]. To analyse the structural behaviour of SFS under external loads, various methodologies have been introduced. C. J. Gantes uses the equilibrium continuum to approximate the displacement of a 2D scissor plane structure (SPS) and a 3D scissor frame structure (SFS). Furthermore, A. Kaveh et al. [22] and W. Shan et al. [23] developed stiffness matrices for duplet (a scissor unit) and uniplet (scissor members), which can be integrated with conventional stiffness matrix to determine the structural integrity. T. Kokawa [24] proposed another approach to simplify structural analysis by reducing the degrees of freedom from 10 to 2, utilising an equivalent spring model to represent the scissor loop. Although extensive research on structural analysis has been conducted on SFS under various load conditions, some critical aspects remain underexplored. One such aspect is the structural performance of the linkages in additional locking mechanisms. These connections often exhibit inherent weaknesses, making them structurally unfavorable when subjected to external loads. However, when performing structural analysis, many designers tend to over-constrain the nodes, making them overly rigid. This approach often leads to overestimating the structural integrity of the overall structure, resulting in designs that may not be sufficiently robust. Additionally, imperfections caused by fabrication and installation can further exaggerate these issues, reducing structural stiffness and leading to lower failure load factors [14]. While much research has focused on modeling and structural analysis for typical load conditions, the effects of loads acting on the locking mechanisms of SFS remain unproven and not validated against FEM models in the literature. This highlights the need for further experimental studies to validate theoretical models and understand the actual performance of SFS.

The focus of this study is to conduct experimental and numerical investigation on a proposed SFS enhanced with additional manual locking members. The experimental results of displacement and stress measurements at critical points on the scissor members are compared to three proposed SFS FEM models: standard rigid modelling, considering imperfections, and completely removing the locking mechanism. This comprehensive discussion identifies and showcases the structural behaviour of the SFS and highlights the crtitical condition when the loading is applied directly to the locking mechanism linkage, emphasising the importance of accurate modelling techniques.

2. Methodologies

This section comprehensively explains the assembly of the experimental specimens, the experimental design and procedure, and the data analysis plan. The details of the SFS FEM model and the three proposed SFS FEM models for validation were also included in this section.

2.1. Experimental specimens specifications

The experimental specimens from Table 1 was assembled utilising steel sections with steel grade of S 275. The Young's modulus, E, Poisson's ratio, ν, and density, ρ, of the designated steel are 210000 N/mm^2, 0.3, and 7850 kg/m^3, respectively. To improve the scalability of the results given a total applicable loading of 1500 N, smaller steel sections were utilised. Rectangular and square hollow steel sections (RHS and SHS) were selected for the scissor members due to their even stress distribution. Using SHS simplifies stress validation by recalculating the bending moment on the section surface based on the strain gauge measurements. Table 1 provides the lists of scissor frame structures with their specimen IDs, cross-section names, structural frame depths.

Table 1
List of specimens and their structural member cross-section

Specimen ID	Cross-Section Name	Frame Depth, h (mm)	Area, A (mm^2)	Moment of Inertia, I (mm^4)
SS-SHS25251.8-0.50	SHS 25 × 25 × 1.8 mm thk.	500	167	15074.81
SS-SHS25251.8-0.25	SHS 25 × 25 × 1.8 mm thk.	250	167	15074.81
SS-RHS50251.8-0.50	RHS 50 × 25 × 1.8 mm thk.	500	257	82266.39
SS-SHS25252.5-0.50	SHS 25 × 25 × 2.5 mm thk.	500	225	19218.75

The configuration of the SFS was built with two sets of SPS, each consisting of a chain of three translational units connected by a series of linkages as illustrated in Fig. 1(a). This configuration was chosen for its standardised scissor member fabrication, facilitating repetitive production. In the SFS, the additional locking mechanism was added by assembling four bars bolted to a multipurpose linkage shown in Fig. 1(a) enhancing the stiffness and rigidity of the SFS. To adjust the frame depth, the length of the bars for the locking mechanism can be calculated and predetermined before fabrication. When the SFS is in the undeployed state, the locking mechanism are free to rotate, accommodating the movement of the group of scissor members. Upon deployed to the predetermined frame depth, the movement of the scissor members is structed by the locking mechanism. Pre-drilled bolt holes on the locking mechanism linkage and the bars allow for additional manual bolt insertion, fixing the connection and the entire structure in place. The process of deployment of the locking mechanism is illustrated in Fig. 1(b). To improve the the effectiveness of the proposed SFS, snap-fit fasteners can be design and applied to the structure [25]. The strength and capacity of these snap-fit fasteners can be further studied for use in high load-bearing applications. However, in this experimental study, simplified steel bolts were used for manual locking purposes. Based on the schematic drawing shown in Fig. 2, a series of connection linkages were fabricated to join all translational units from various axis directions and the locking mechanism together to form a manual locking SFS.

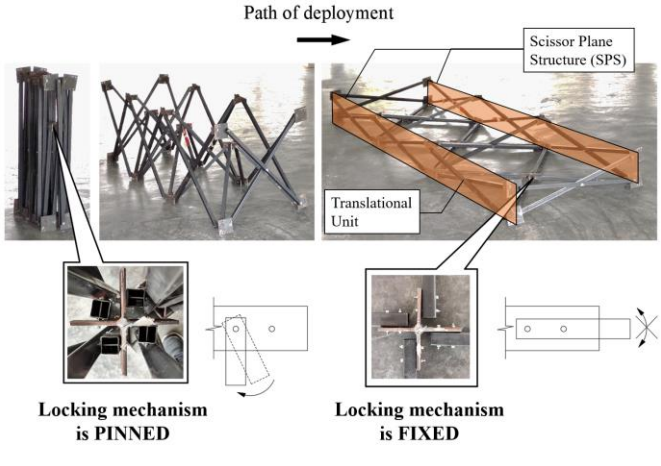

(a)

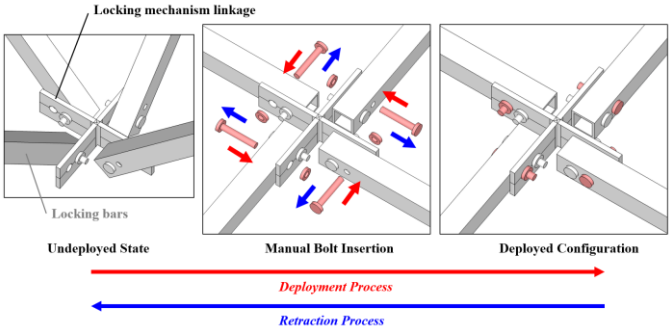

(b)

Fig. 1 Illustration of (a) an actual SFS model and its deployment process, and the (b) simultaneous deployment process of a locking mechanism

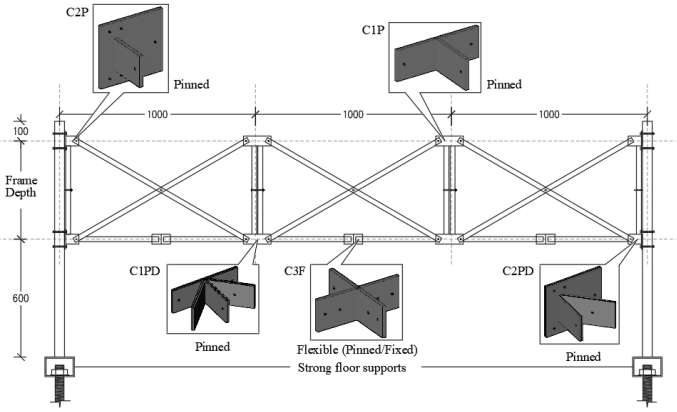

(a)

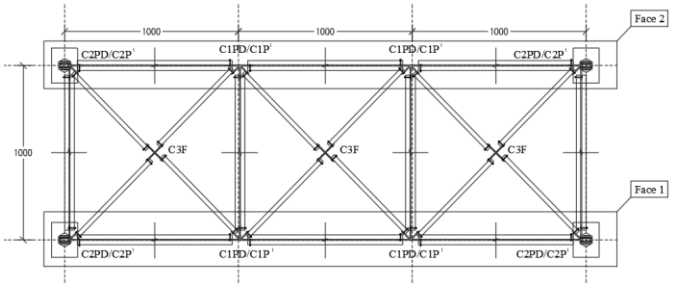

*Note:
1BOT/TOP connection linkage label

(b)

Fig. 2 Dimension and details of the SFS and connection labels shown in (a) elevation view and (b) plan view

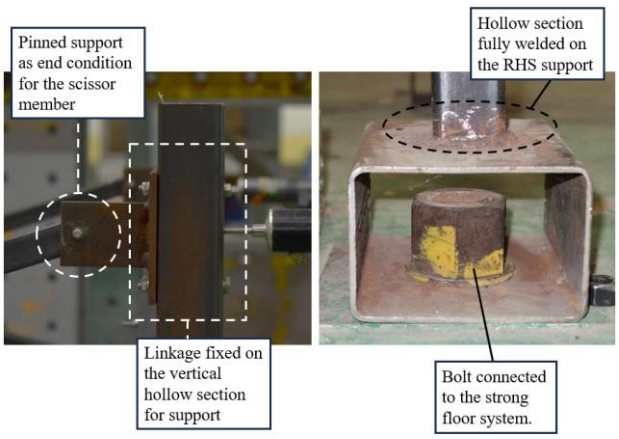

Fig. 3 Illustration of vertical hollow section support and the floor support system for SFS

The support for the SFS was fabricated to simulate the steel columns that hold the SFS in place. The SFS was connected to these column at four corners as shown in Fig. 2. The steel members used for the support columns were SHS

50 × 50 × 4.0 mm thk. Additionally, the support was designed to connect to the strong floor system in the laboratory, ensuring that the support members were fixed in the positions shown in Fig. 3.

For the purpose of this study, the SFS was subjected to manual continuous loading with several 5 kg (approximately 50 N) plate at each point of interest. The loading points were set at the center of each C3F mentioned in Fig. 2, which are at the center of the locking mechanism linkage. Each loading point was subjected to a m,aximum load of 500 N, resulting in an overall maximum total load of 1500 N on the SFS. The application of load at the locking mechanism linkage allows the investigation to verify the effectiveness of the locking mechanism after loading. When the SFS is loaded, it experiences a vertical displacement, hence a clearance of 600 mm between the SFS and the floor was provided as planned in Fig. 2. An illustration of the experiment under loading is shown in Fig. 4. When the load was applied to the SFS, the stress is distributed throughout the scissor members.

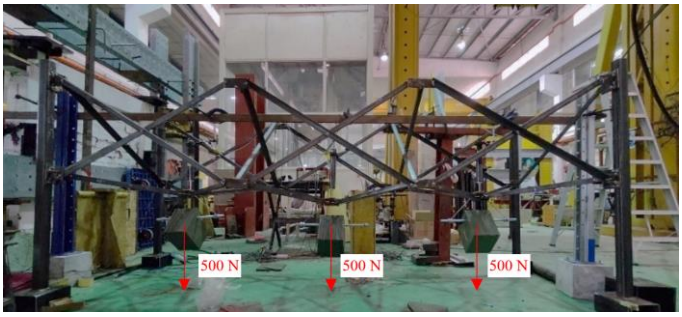

(a)

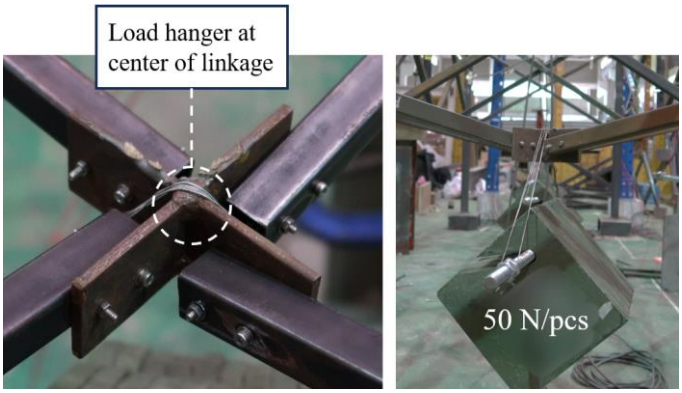

(b)

Fig. 4 Illustration of loading scenario during the experiment for (a) overall view and (b) close-up view

Linear Variable Differential Transformers (LVDTs) and strain gauges were employed to measure displacement and strain in the scissor members. An LVDT with a 100 mm measurement range was used to measure displacement from the SPS under loading condition. The positions of the LVDTs and its actual setup are shown in Fig. 5. To account for uncertainties in the experimental testing, the LVDTs were vertically aligned during the setup. Furthermore, the LVDTs were positioned so that only half of their range (50 mm) was used to obtain measurements in the positive or negative directions.

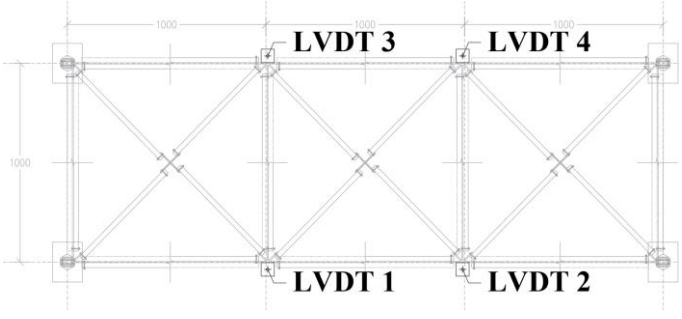

(a)

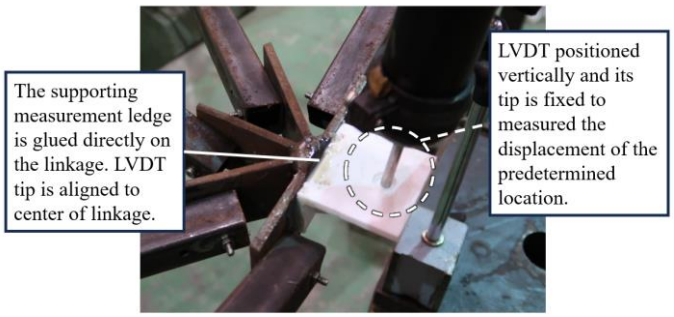

(b)

Fig. 5 Illustration of (a) predetermined location of LVDTs and its (b) actual setup

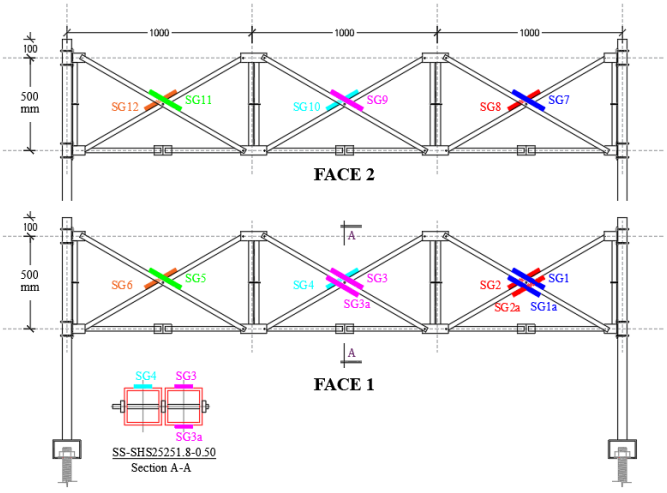

(a)

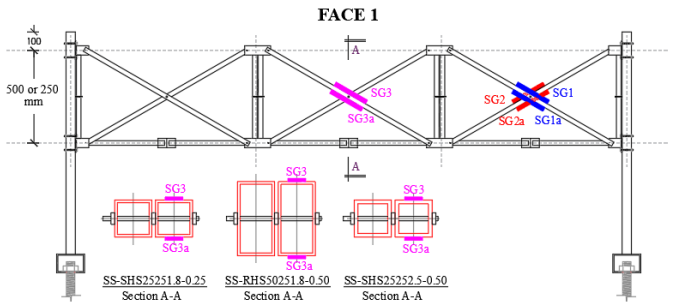

(b)

Fig. 6 Location of strain gauges of (a) SS-SHS25251.8-0.50 and (b) others

2.2. Experimental design and procedure

The experiment was conducted in a structural lab equipped with a strong floor system to provide robust support for the specimen. Before the test, the SFS was carefully set-up, ensuring the proper placement of the load hanger, LVDT, and strain gauge as mentioned in Section 2. The data logger readings from the LVDT and strain gauge were zeroed before the start of the test to establish a baseline reference.

The test began by continuously placing the load plates (50 N) at the designated load points. The deflection of the structure was observed, and a waiting time of 30 seconds was employed before data collection, as recommended by J. P. Valcarcel et al. [26] in a similar load tests. The data collected included the displacement of the SFS (measured by LVDT) and the strain at critical points in the scissor members (measured by strain gauge). The loading process was repeated until a load of 500 N was reached at each load point. Once this load was achieved and the corresponding data was recorded, the load plates were gradually retracted to measure the displacement and strain during the unloading phase. The entire experiment was repeated at least twice on the same specimen to account for permanent displacement of the SFS due to initial structural set.

The same testing procedure was performed on the following three specimens. For SS-SHS25251.8-0.50, the overall stress behaviour throughout the SFS were being analysed to validate the symmetrical of the structure. Furthermore, comparison between the stress and displacement results of all specimen mentioned in Table 1 will be compared and discussed.

2.3. Experimental results analysis

The stress verification was conducted to study the stress behaviour at critical location on the scissor members as shown in Fig. 6. The SFS was fabricated symmetrically, allowing cross-checking of the stress around the structure. The symmetrical equivalent stress locations are noted to be SG 1, SG 6, SG 7, SG 12; SG 2, SG 5, SG 8, SG 11; SG 3, SG 4, SG 9, SG 10.

It was assumed that the stress distribution within the hollow steel section remained uniform under the applied loading as shown in Fig. 7. The experiment results indicated that the scissor members remained in the elastic zone under the total applied loading of 1500 N. Additionally, the neutral axis shift was not considered since the members were still behave elastically due to the small load [27]. Utilising the fundamental bending stress formula in Fig. 7, the bending moment experienced by the scissor members under the applied loading was calculated by multiplying the assumed elastic modulus and section modulus with the strain obtained from the strain gauges in the experiment. With the data extracted from the experiment, the bending moment diagram of the SFS can be obtained.

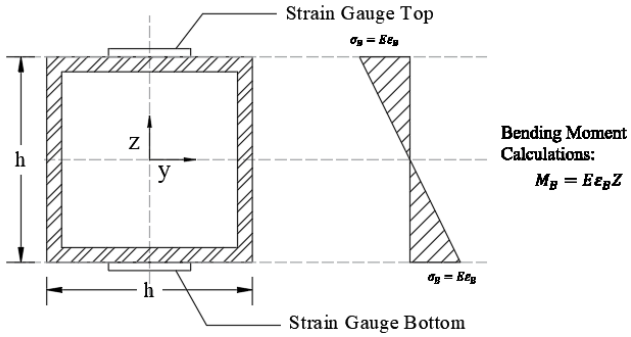

*Note:
σ_B is bending stress, E is young modulus, M_B is bending moment, σ_B is bending strain, Z is section modulus.

Fig. 7 Elastic stress profile in the cross-sections

In overall, total of four specimens were being compared of their stresses and displacment measured. The comparison involved assessing the overall maximum deflection observed at the SPS and determining the structure's stiffness using the best-fit line (trendline) function in Microsoft Excel. For the stress result comparison, the analysis aimed to identify the most influenced point when the cross-sectional properties of the scissor member were modified. This approach provides a comprehensive understanding of how variations in cross-sectional propertiues impact the stress distribution and overall structural performance of the SFS.

2.4. FEM Modelling

In this study, SCIA engineer software was employed to model the experimental specimens of the SFS with their material and mechanical properties were as mentioned in Section 2.1. The purpose of the FEM modelling analysis was to compare the results of three different FEM models to the experimental results where the load acts on the center of the locking mechanism linkage. The three FEM models consists of FEM 1, FEM 2 and FEM 3. Where, FEM 1 is the standard FEM model, which includes the locking mechanism and has no imperfections introduced in the SFS; FEM 2 introduces imperfections in the SFS; while FEM 3 excludes the locking mechanism from the SFS. Consequently, FEM 1 serves as the control model for all comparisons in this analysis.

2.4.1. FEM 1 model: Standard modelling

The base model of FEM 1 includes several key properties: a pinned connection as the beam end condition for the scissor member, a pivotal joint, a locking mechanism linkage, and a pin supported point on the strong floor. The standard modelling diagram of the SFS for FEM 1 is presented in Fig. 8, with additional modelling details is explained consecutively in Table 2.

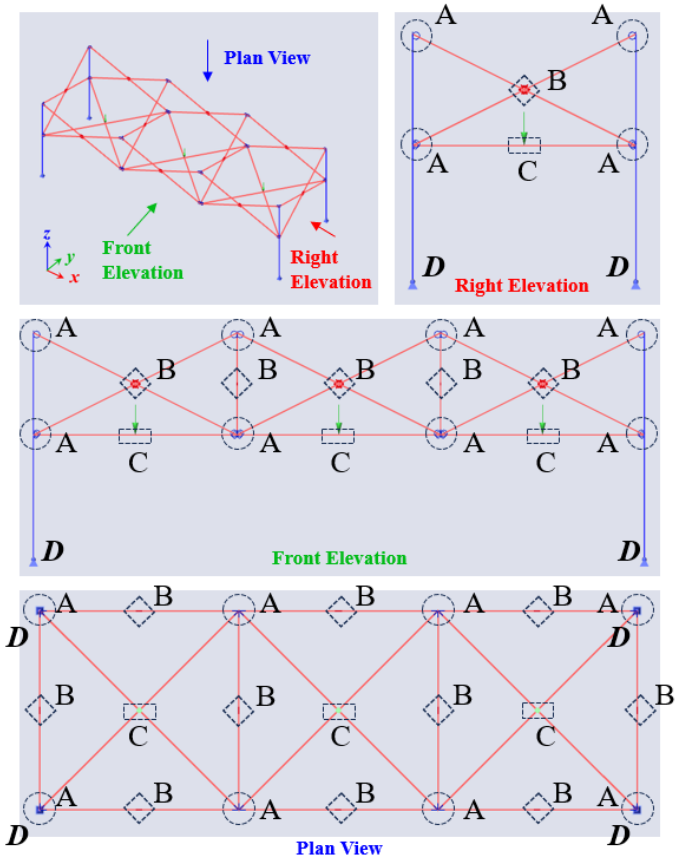

Fig. 8 Wireframe diagram of FEM 1 base model with labels

Table 2
Modelling boundary conditions of the SFS with labels from Fig. 8

Notation	Modelling	Remark
A	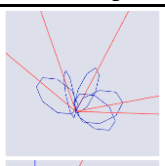	End conditions of scissor members are pinned joints, allowing rotation about the major axis of the scissor member.
B	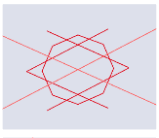	Unique cross-link plugin that allows separation of rotation ry of each adjacent scissor member while constraining other degrees of freedom. Functions similarly to a pivotal defined master/slave node constraint.
C		Load acting on the intersecting node of the locking mechanism. The node of the locking mechanism connects the locking bars rigidly at the intersection. Refer to Fig. 1, for the locking mechanism concept.
D	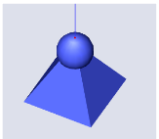	Pinned connection below the vertical supporting members to simulate the support condition on the strong floor.

One of the most challenging aspects of the SFS is modelling the pivotal point. The pivotal joint is crucial in an SFS because its location can significantly alter the deployment behaviour, whether translational or polar. However, modelling the pivotal joint is modelling the pivotal joint is not as straightforward as defining a typical pinned node on the intersecting point. The boundary conditions of the pivotal joint are illustrated in Fig. 9.

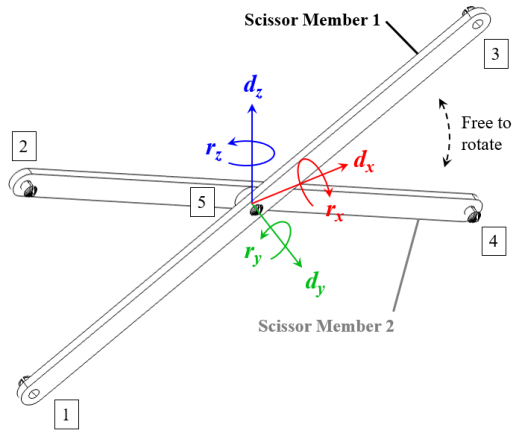

Fig. 9 3-D Local axis of pivotal joint of a scissor unit

In Fig. 9, the variables d_x, d_y, and d_z represents the displacement of the node of each scissor member at the pivotal joint along the x, y and z axes, respectively. Similarly, r_x, r_y, and r_z denote the rotation of the node of each scissor member about the x, y and z axes, respectively. At the pivotal point, it is important to note that the displacement d_x, d_y, and d_z of both scissor members will always move in the same direction, as they are constrained by each other with a pin. A unique property of the pivotal point in the SFS is that r_y is free to rorate for each connected scissor member 1 and 2, whereas r_x and r_z remain constant. Furthermore, the scissor member remains continuously connected from node 1 to node 5 to node 3 for scissor member 1 and from node 2 to node 5 to node 4 for scissor member 2. Thus, the modelling of the pivotal joint constraint should include these features to accurately capture the behaviour of the scissor members in the model. Fig. 10 illustrates the load cases affecting the SFS, with their response to the applied load indicated by the blue dashed line.

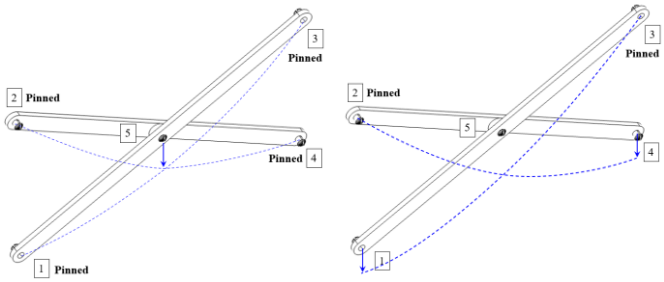

(a) (b)

Fig. 10 A scissor unit under various load at (a) center of the pivotal point and at (b) Point 1 and Point 4.

At Fig. 10(a), the load is applied directly on the pivotal point of the scissor member with the pinned supports are defined at point 1, 2, 3 and 4. At Fig. 10(b), the load is applied on point 1 and 4 where the pinned support is defined at point 2 and point 3. In both load cases, the adjacent scissor members will transfer shear force along the xz plane when the load is applied, causing them to bend about the pivotal point. To capture this behaviour in the modelling, a master-slave node approach [28] can be used to define the constraint between both scissor member at the pivotal point. The boundary condition of this mid-beam connection is to constrain the degree of freedom of d_x, d_y, d_z, r_x and r_z of both scissor members. Meanwhile ry of both scissor members remains freely rotatable.

2.4.2. FEM 2 model: Standard modelling incorporating imperfection due to Fabrication and Installation offsets.

During the fabrication of the SFS, achieving high accuracy is crucial to obtain the desired deployed and retracted states. Therefore, the dimensions of the SFS should be fabricated as precise as possible. However, due to workmanship and human error, especially in large structures, fabrication errors are inevitable.

In this study, imperfections due to workmanship were calculated under the assumption that the locking bar has a fabrication error of 0.5% at both ends of the structure. The error includes the bolt hole were not aligned at the desired location, which lengthen the open span of the locking bar. As illustrated in Fig. 11, even slight errors in the structural dimension can accumulate, resulting in imperfections up to 81 mm. To account for these imperfections, the modelling in this study rounded the imperfection up to a whole number of 100 mm. This conservative approach ensures that the model covers a wider range of potential deviations, providing a safety margin that enhances the robustness and reliability of the analysis.

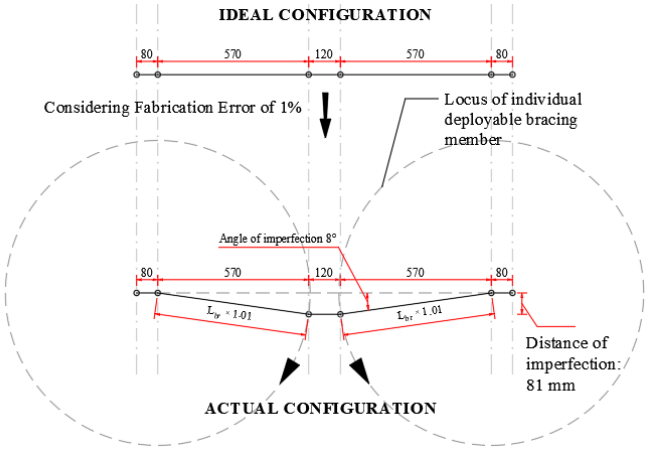

Fig. 11 A scissor unit under various load at (a) center of the pivotal point and at (b) Point 1 and Point 4

2.4.3. FEM 3 model: Standard modelling without consideration of locking mechanism.

For this configuration, the locking mechanism was removed from the SFS. Despite this removal, the SFS was still able to carry the load since it is still pinned connected to the vertical hollow sections for support. The load in this case was assumed to be equally distributed among all the nodes where the locking mechanism would normally connect. The purpose of this configuration is to identify the behaviour of the SFS when subjected to external loads without the presence of the locking mechanism. While the locking mechanism is removed from the modelling, it is assumed that the load is transferred equally to each point on the modelling of the SFS. The structural model elevation and 3D view is shown in Fig. 12.

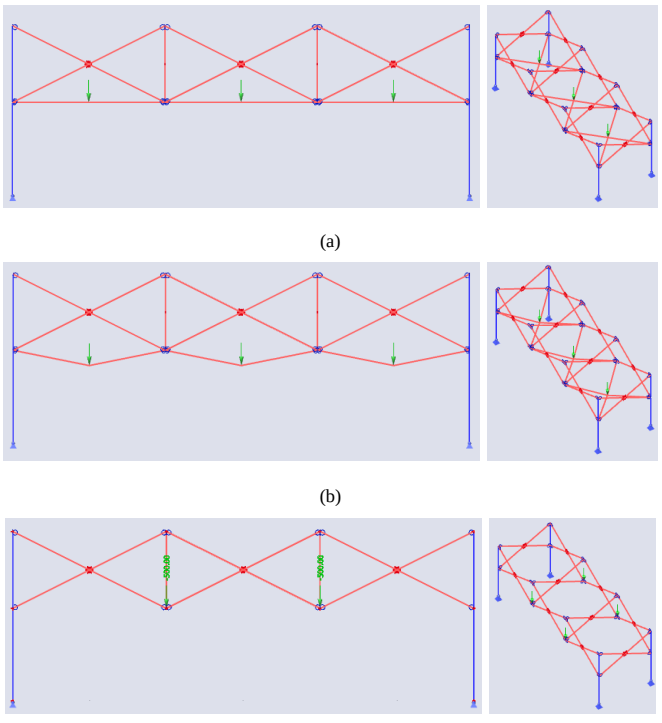

(a)

(b)

(c)

Fig. 12 Illustration of three modelling of SFS (a) FEM 1, (b) FEM 2, and (c) FEM 3

3. Results and discussions

This section summarises and discusses the load test results on the SFS.

Several key findings and observations were obtained from conducting the experimental tests and analysing the collected data sets. These findings offer valuable insights into the structural behaviour of the SFS. Additionally, a numerical comparison with the experimental results will be conducted for validation, ensuring the accuracy and reliability of the model.

3.1. Stress distribution measured in SFS.

Based on the strain gauge results, measurements were obtained that reflect the surface strain at the attachment points. For this analysis, the strain values were converted to stress, assuming an elastic modulus of 210000 N/mm² for the steel. As shown in Fig. 13, the behavior of all calculated stresses for SS-SHS25251.8-0.50 was consistent. The figure shows that the stress for the first set is negative, the second set is positive, and the third set is negative. Positive stress values indicate tensile stress, while negative values represent compressive stress. Based on Fig. 13, the highest calculated stress for SS-SHS25251.8-0.50 is -78.96 MPa, measured at Face 2.

When adjacent scissor members are connected to each other with a pivotal joint, they connect at different planes, as depicted in Fig. 9. However, despite the offsets of each scissor member at the pivotal connection, the results of the strain gauges placed at the top and bottom of the scissor member at the pivotal point show symmetrical behavior, as shown in Fig. 13, with the stress calculated for the top and bottom sections having opposite signs, represented by the solid and dashed lines, respectively. This symmetrical behavior is demonstrated by the ratio difference tabulated in Table 3, where values closer to 1.0 indicate symmetry in the scissor member. At the pivotal point of the scissor member, when tensile stress is on the top and compressive stress is on the bottom, the scissor member experiences a hogging moment at that location, and vice versa. Hence, the SFS can be modelled as a 2D member in the software with a clear definition of the boundary conditions discussed in Section 2.4.1.

According to Fig. 13 and Fig. 14, it is evident that all results align in terms of the sign of the stress found at the top of the scissor member. At SG1/SG1a and SG3/SG3a, the SFS experiences a sagging moment, while at SG2/SG2a, the scissor member experiences a hogging moment when subjected to loading. Therefore, when an SFS is subjected to loading, the scissor member connected to the top of the supporting part will experience a hogging moment induced by the shear force from the adjacent scissor member. Differences in the strain gauge readings may also be caused by the sensitivity of the gauges. Given the small magnitude of the loading, the strain gauge values may vary significantly; however, the consistency of the readings indicates that the SFS is symmetrical and performs as expected.

Another notable observation is that the gradient of the curve is relatively straight, indicating that the scissor member is still behaving within the elastic zone. Additionally, the scissor members exhibit no nonlinear attributes, resulting in the linear graph plotted in Fig. 14. Therefore, the analysis shows that the SFS behaves linearly during the static deployed state when subjected to loading, despite its unique flexible properties.

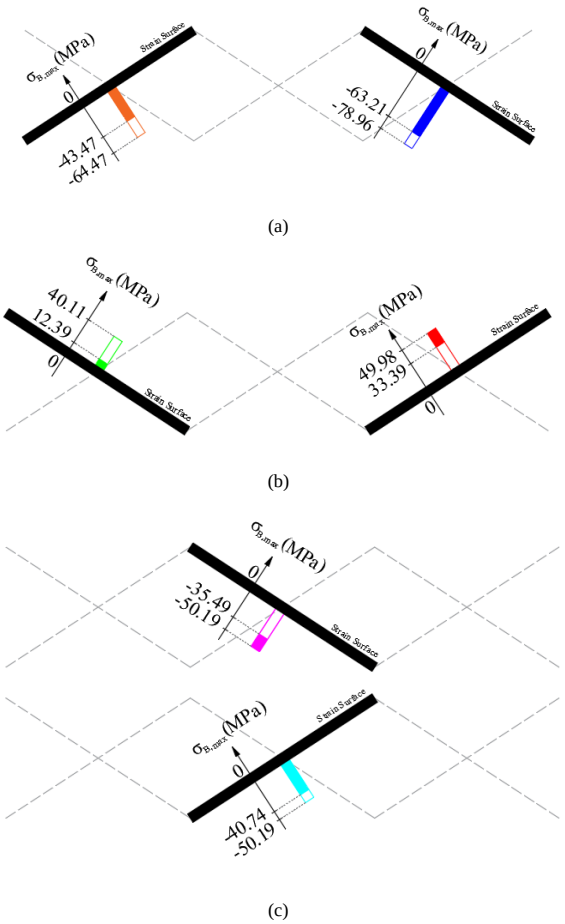

*Note:
[1]Solid fill represents strain gauge reading at Face 1
[2]No fill represents strain gauge reading at Face 2
[3]Strain surface directly the surface of the strain gauge measuring the data.

Fig. 13 Illustration of the calculated stresses depicted on the SFS schematic diagram for (a) Set 1: SG1, 6, 7, 12; (b) Set 2: SG 2, 5, 8, 11; and (c) Set 3: SG 3, 4, 9, 10 symmetrical members

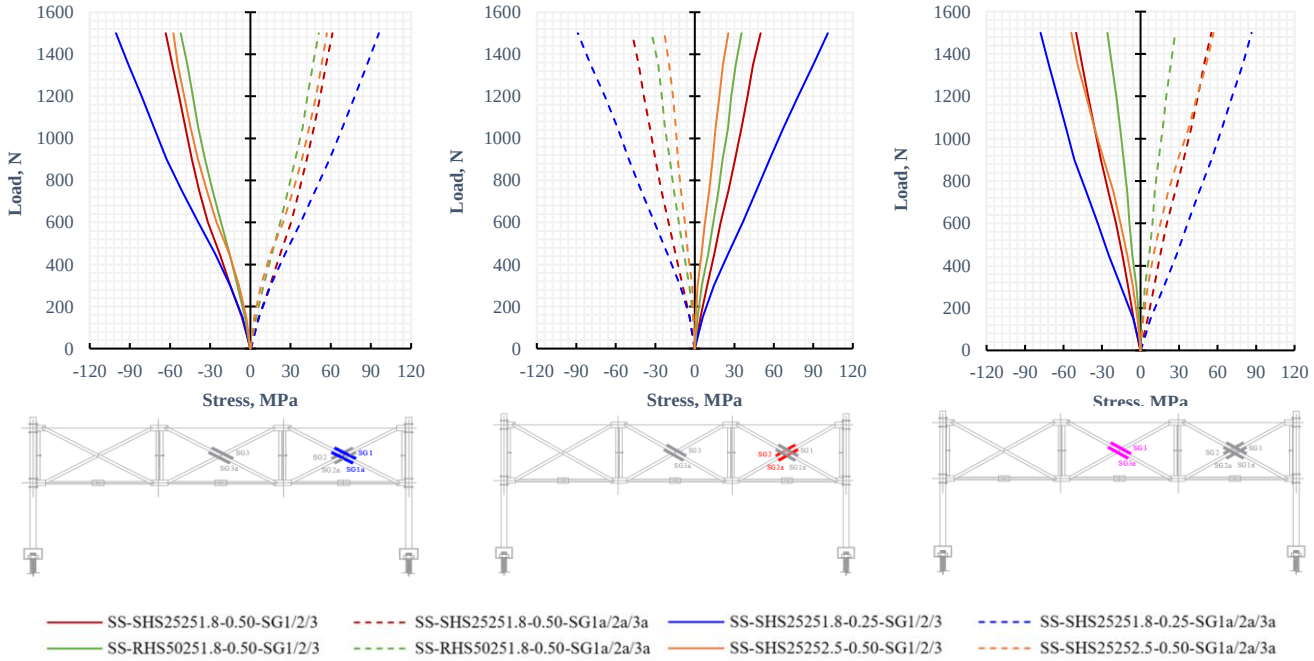

Fig. 14 Load vs stress curve of the SFS measured at (a) SG1/SG1a, (b) SG2/SG2a and (c) SG3/SG3a

Table 3
Critical stress of scissor member under 1500 N

Specimen ID	Critical Stress at 1500 N, MPa						Ratio Difference			Calculated Bending Moment, Nm			Load/ Weight Ratio, N/kg
	SG1	SG1a	SG2	SG2a	SG3	SG3a	SG1/ SG1a	SG2/ SG2a	SG3/ SG3a	M_1	M_2	M_3	
SS-SHS25251.8-0.50	-63.21	61.32	49.98	-47.67	-50.19	55.23	1.03	1.05	0.91	74.91	-58.74	63.42	44.49
SS-SHS25251.8-0.25	-100.38	95.97	101.01	-88.83	-77.91	86.52	1.05	1.14	0.90	118.12	-114.20	98.92	48.12
SS-RHS50251.8-0.50	-52.08	51.03	35.49	-32.76	-25.83	27.09	1.02	1.08	0.95	169.15	-111.96	86.82	28.68
SS-SHS25252.5-0.50	-57.54	57.12	25.41	-23.1	-53.97	56.91	1.01	1.10	0.95	87.80	-37.15	84.91	33.63

The critical stress of the scissor member at 1500 N was recorded in Table 3. The table shows that the specimen SS-SHS25251.8-0.25 has the highest stress among all the participating specimens that are at SG1 which is -100.38 MPa, followed by SS-SHS25251.8-0.50, SS-SHS25252.5-0.50, and finally SS-RHS50251.8-0.50, with stress value of -63.21 MPa, -57.54 MPa, and -52.08 MPa respectively. Based on observations, it was noted that a reduced depth increases the bending stress that each member must resist during the static stage. However, while calculating the bending moment based on the fundamental bending stress equations, it was found that SS-RHS50251.8-0.50 yields higher bending moment results. This is due to the fact that the cross-sectional area of SS-RHS50251.8-0.50 provides a higher moment of inertia compared to the other scissor members, increasing the section modulus and the stiffness of the scissor member, which in turn increases the calculated bending moment. Additionally, the calculated bending moments shown in the table indicate that M_1 always has the highest bending compared to other critical locations. This critical bending moment is attributed to several factors, including the pin-connected end support and the direct loading by adjacent scissor members, which introduce high shear forces at the pivotal point of the SFS, resulting in significant bending at that location. Therefore, in the structural analysis and design of the SFS, special care must be taken with the scissor member at the end support, as it will have to resist higher internal forces compared to the scissor units at the center of the structure. Finally, utilizing the experimental data, the bending moment diagram can be drawn as shown in Fig. 15.

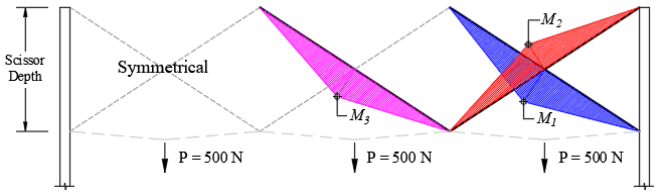

*Note:
M_1, M_2, M_3 value represents the calculated bending moment in Nm based on their signs, with values taken from Table 3. Negative values are accounted for in the figure to depict hogging moment at M_2 in the SFS.

Fig. 15 Typical bending moment diagram for all SFS

3.2. Displacement analysis of SFS.

Shown in Fig. 16 are the displacements of the SFS specimens recorded by the LVDT in the experiment. It was observed that despite the high flexibility of the SFS, the displacement response under load remains linear. Comparison between all the specimens shows that the SFS with the cross-section having the highest properties of area and moment of inertia, SS-RHS50251.8-0.50, has the highest stiffness among all the specimens, with k equal to 430.12 N/mm. This is followed by SS-SHS25252.5-0.50, SS-SHS25251.8-0.25, and finally SS-SHS25251.8-0.50, with stiffness measured at 253.96 N/mm, 168.55 N/mm, and 165.29 N/mm, respectively. The best-fit line shows a very high r^2 value, indicating that the data points closely agree with the best-fit line and confirming the linear displacement behavior of the SFS.

Further analysis of the displacement, as shown in Fig. 16, includes another line connecting the data points in addition to the best-fit line. It was found that the line connecting the data points at the initial stage shows the SFS exhibiting slightly stiffer behavior at the start of the loading stage. The initial stiffness of the SFS is largely due to the joints of the SFS. When lightly loaded, the joints retain some degree of fixity, providing very small moment resistance and slightly increasing the stiffness of the SFS at the initial stage, approximately from 0 N to 800 N. In an ideal scenario, pin connections are assumed to have no moment resistance, meaning they allow rotation without resisting it. However, in practical situations, real-world pin joints may not be perfectly frictionless or free of any resistance. The slight resistance can provide a small amount of moment resistance at the initial stages of loading at the joint, increasing the stiffness of the whole structure slightly. This phenomenon occurs due to factors like friction within the pin joint, the imperfect fit of the pin, or slight deformation of the joint components under load, which can create a temporary semi-rigid behavior. As the loading increases, these minor resistances are overcome, and the joints transition to their expected behavior as fully pinned connections. At this point, the joints no longer provide significant moment resistance, and the SFS's stiffness returns to what is expected for a pinned system. This transition from semi-rigid to fully pinned behavior results in the observed reduction in stiffness as the load increases beyond the initial stage.

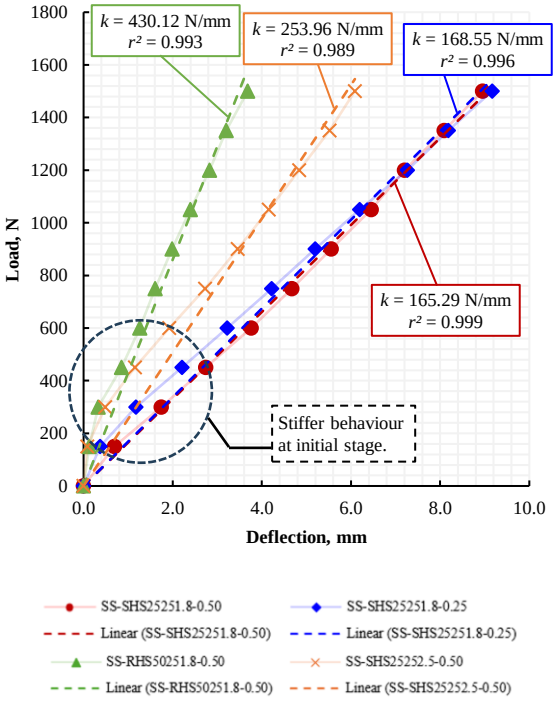

*Note:
Dashed line indicate the best-fit line based on the displacement data from 0 N load to 1500 N load.
Where,
k is the stiffness of the SFS calculated by the gradient of the best-fit curve
r^2 is the degree of best fit of the data points to the line, with 1.0 being very compatible and 0.95 to be the acceptance limit of the compatibility.

Fig. 16 Graph of displacement vs applied load for all SFS

Furthermore, when comparing the critical stress from Table 3 with stiffness from Fig. 16, it was shown that changing the cross-section of the scissor member did not result in significant differences in stress distribution. Instead, when the depth of the SFS is reduced, the stress experienced by each scissor member increases significantly, as noticeable when comparing SS-SHS25251.8-0.50 to SS-SHS25251.8-0.25. The greatest difference between them is at SG2, where the ratio difference of the 250 mm to the 500 mm scissor depth is 2.02. When the depth of the SFS reduces, the load-to-steel weight ratio of the SFS increases. The load-to-steel weight ratio of SS-25251.8-0.25 is 48.12 N/kg, the highest among the specimens. As load/weight ratio increases, fewer steel members are present to resist the same load, causing stresses on scissor members to increase.

However, on the other hand, when the section properties of the cross-section increase, the stiffness of the SFS also increases. For instance, the specimen SS-RHS50251.8-0.50, which has greater section properties such as area (A) and moment of inertia (I), achieved a stiffness of 430.12 N/mm. The load-to-steel weight ratio of this specimen is the lowest, at 28.68 N/kg. As the section properties of a section increase, its structural stiffness also increases, allowing for greater capacity and displacement. Hence, further study should be proposed to account for the stress and stiffness behavior of the SFS to determine the optimum configuration for the SFS.

By compiling the displacement data from Fig. 16 and the stress data from Table 3, the load capacity of the SFS before the scissor member starts to experience yielding can be approximated, assuming the yield stress, f_y of the steel section is 275 N/mm² and the structure behaves linearly. The calculation of the predicted maximum load is shown in Table 4. The predicted maximum load up to 275 N/mm² stress is calculated based on the critical stress from the experiment using the ratio method. Whereas, the predicted maximum load up to the displacement limit of National Annex of MS EN 1993-1-1 [29] was calculated based on the stiffness measured from the experiment. According to MS EN 1993-1-1, the allowable displacement for the SFS for a 3.0 m span is 15 mm. In Table 4, the displacement of the SFS specimen is calculated accordingly and it was found that, based on the displacement limit by MS EN 1993-1-1, the predicted maximum load $P_{d,max}$ shows lower load compared to $P_{\sigma,max}$. Hence, from this result, it can be noted that the stiffness of the SFS greatly governs the design of the SFS.

Table 4
Summary of specimen's stiffness and critical stresses and their predicted capacity

Specimen ID	Stiffness, k (N/mm)	Critical Stress at 1500 N	Predicted Maximum load up to 275 MPa stress, $P_{\sigma,max}$ (kN)	Predicted maximum load up to MS EN 1993-1-1 displacement limit [29], $P_{d,max}$ (kN)
SS-SHS25251.8-0.50	165.29	62.27	6.62	2.48
SS-SHS25251.8-0.25	168.55	98.18	4.20	2.53
SS-RHS50251.8-0.50	430.12	51.56	8.00	6.45
SS-SHS25252.5-0.50	253.96	57.33	7.20	3.81

3.3. Experimental results comparison with FEM modelling

Three FEM models were developed to compare their results with the experimental results. The data from these comparisons are tabulated in Table 5. Furthermore, based on the data in Table 5, Fig. 17 was plotted to illustrate the closeness of the experimental data to the numerical modeling results.

Table 5
Tabulation of compilation and comparison of experimental and FEM results

Parameters	Specimen ID	Results			
		EXP	FEM 1	FEM 2	FEM 3
d, mm	SS-SHS25251.8-0.50	8.95	2.47	6.19	10.54
	SS-SHS25251.8-0.25	9.17	2.12	6.36	7.41
	SS-RHS50251.8-0.25	3.68	0.97	1.45	2.1
	SS-SHS25252.5-0.25	6.09	2.11	4.94	8.3
	Best-fit gradient (mm/mm)	-	**3.63**	**1.42**	**0.92**
M_1, Nm	SS-SHS25251.8-0.50	74.91	21.34	41.65	100.05
	SS-SHS25251.8-0.25	118.12	16.2	52.65	74.43
	SS-RHS50251.8-0.25	169.15	37.64	53.55	105.87
	SS-SHS25252.5-0.25	87.8	22.58	42.5	100.21
	Best-fit gradient (Nm/Nm)	-	**4.49**	**2.41**	**1.17**
M_2, Nm	SS-SHS25251.8-0.50	-58.74	-10.22	-44.9	-71.17
	SS-SHS25251.8-0.25	-114.2	-11.47	-70.42	-81.58
	SS-RHS50251.8-0.25	-111.96	-8.83	-39.06	-64.53
	SS-SHS25252.5-0.25	-37.15	-10.07	-44.38	-70.56
	Best-fit gradient (Nm/Nm)	-	**7.88**	**1.60**	**1.12**
M_3, Nm	SS-SHS25251.8-0.50	63.42	19.94	62.22	76.94
	SS-SHS25251.8-0.25	98.91	21.05	61.59	58.92
	SS-RHS50251.8-0.25	86.82	48.53	76.54	83.17
	SS-SHS25252.5-0.25	84.91	22.26	63.09	77.32
	Best-fit gradient (Nm/Nm)	-	**2.56**	**1.26**	**1.10**

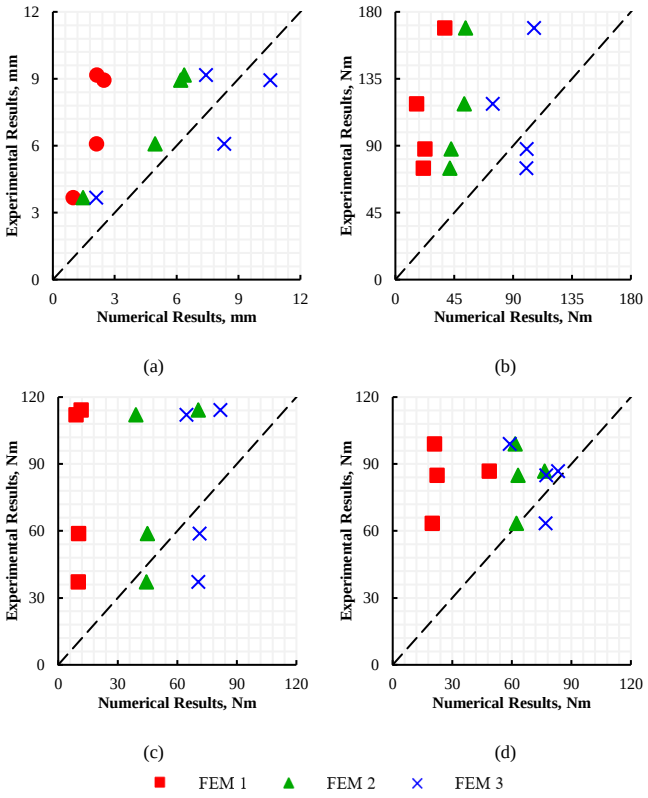

Fig. 17 Comparison graph of experimental data and numerical data for the (a) displacement, (b) M_1, (c) M_2, and (d) M_3

In Fig. 17, the numerical and experimental results were plotted on a graph where the black dashed line represents the 1:1 ratio between the experimental and numerical model results. If the data points are above the black dashed line, the experimental results are higher than the numerical results. Conversely, if the data points fall below the black dashed line, the numerical results are higher than the experimental results. Additionally, the best-fit gradient is calculated from the best-fit line with an additional point at (0,0) was added to each data set, representing zero values for both the experimental and numerical results. The best-fit line was not drawn in the figure to avoid confusion; instead, the gradient values were listed in Table 5 for more comprehensive discussion and comparison.

According to Table 5, FEM 1 shows the highest gradient difference among the modeling configurations for all the parameters which are 3.63, 4.49, 7.88, and 2.56 for d, M_1, M_2, and M_3 respectively. FEM 1 is the standard FEM model for the SFS with loading acting at the center point of the locking mechanism linkage. Although the locking mechanism linkage was fixed with pinned joint connections as shown in Fig. 1(b), this does not ensure that the joint is rigid and continuous. Compared to the experimental results, the FEM 1 model yields smaller results, indicating that it overpredicts the stiffness of the SFS.

In FEM 2, initial imperfections due to fabrication and assembly of the SFS are considered. The results from FEM 2 are closer to the experimental results, which are 1.40, 2.41, 1.60, and 1.26 for d, M_1, M_2, and M_3 respectively, nearly twice more accurate than the results from FEM 1. However, the experimental results are still higher than the numerical results. FEM 3 shows the closest results to the experimental data, as indicated by a best-fit gradient very close to 1.0. For FEM 3, the best-fit gradients achieved

for the parameters are 0.92, 1.17, 1.12, and 1.10 for d, M_1, M_2, and M_3 respectively. This outcome demonstrates that when the load acts on the locking mechanism, even if it is fixed at the center, the efficiency of the locking mechanism is reduced, rendering it structurally ineffective in the SFS. Therefore, it is crucial to avoid applying load directly to the linkage of the locking mechanism. If necessary, the SFS should be designed to resist the load without relying on the locking mechanism as a structural component. These findings underscore the importance of considering the effects of load application and structural imperfections in the design and analysis of the SFS to ensure accurate modeling and reliable performance.

4. Conclusions

The structural behavior of the scissor frame structures (SFS) under the influence of load at the locking mechanism was investigated through experimental investigation and numerical analysis. Based on the outcomes, several significant findings can be summarised as follows:

1. Stress analysis from the experimental study showed that, although scissor members were connected side by side in two planes, the stress remained symmetrical, allowing for simplified numerical modeling assuming single-plane action.
2. Critical stress was measured at the calculated bending moment M_1, closest to the support, indicating the need for careful design consideration near the support.
3. Altering the cross-section does not significantly affect stress distribution but greatly impacts stiffness. Conversely, changing the depth greatly affects stress distribution. Further study is needed to optimise these features.
4. The resistance of each SFS specimen was calculated based on experimental stiffness and stress, as linear behavior is observed during loading. The deflection limit, according to the National Annex of MS EN 1993-1-1, governs the design, since the predicted maximum load was lower than the predicted maximum load based on the yield strength of steel.
5. Validation of FEM with the experimental model showed that when the load acts directly on the locking mechanism linkage, standard FEM, FEM 1 modeling overpredicts rigidity due to overconstraint.
6. Including linkage imperfections in FEM 2 and FEM 3 significantly improved numerical accuracy, aligning results more closely with the physical model.

Acknowledgement

This work was supported by the Ministry of Higher Education under Fundamental Research Grant Scheme (FRGS/1/2023/TK06/UTM/02/6) and Universiti Teknologi Malaysia (04M87).

References

[1] J. J. Moy, C. S. Tan, S. Mohammad, and A. R. Z. Abidin, "State-of-Art review on deployable scissor structure in construction", Structures, 42, 160-180, 2022.
[2] A. S. K. Kwan, "A Parabolic Pantographic Deployable Antenna (PDA)", International Journal of Space Structures, 10(4), 195-203, 1995.
[3] B. Suthar and S. Jung, "Design and Bending Analysis of a Metamorphic Parallel Twisted-Scissor Mechanism", Journal of Mechanisms and Robotics, 13(4), 040905, 2021.
[4] X. Yu, Y. Yang, Y. Ji, and L. Li, "Experimental Study on Static Performance of Deployable Bridge Based on Cable-Strengthened Scissor Structures", Advances in Civil Engineering, 2021, 4373486, 2021.
[5] C. H. Yan and T. A. Aik, "Design and Analysis of Emergency Deployable Bridge", International Journal of Mechanical Engineering and Robotics Research, 9(10), 1393-1399, 2020.
[6] T.-H. Kim, J.-E. Suh, and J.-H. Han, "Deployable truss structure with flat-form storability using scissor-like elements", Mechanism and Machine Theory, 159, 104252, 2021.
[7] K. Roovers and N. De Temmerman, "Deployable scissor grids consisting of translational units", International Journal of Solids and Structures, 121, 45-61, 2017.
[8] K. Roovers and N. De Temmerman, "Geometric design of deployable scissor grids consisting of generalized polar units", Journal of the International Association for shell and spatial structures, 58(3), 227-238, 2017.
[9] S. Krishnan and Y. Liao, "Geometric Design of Deployable Spatial Structures Made of Three-Dimensional Angulated Members", Journal of Architectural Engineering, 26(3), 04020029, 2020.
[10] V. Beatini *et al.*, "Integration of origami and deployable concept in volumetric modular units", Scientific Reports, 12(1), 19180, 2022.
[11] L. Zhu *et al.*, "Conceptual design and fabrication of modular deployable origami structures for architectural-scale applications", Proceedings of IASS Annual Symposia, 2022(9), 1-8, 2022.
[12] K. K. Vu, J. Y. Richard Liew, and K. Anandasivam, "Deployable tension-strut structures: from concept to implementation", Journal of Constructional Steel Research, 62(3), 195-209, 2006.
[13] Y. Akgün, C. J. Gantes, W. Sobek, K. Korkmaz, and K. Kalochairetis, "A novel adaptive spatial scissor-hinge structural mechanism for convertible roofs", Engineering Structures, 33(4), 1365-1376, 2011.
[14] J. G. Cai, Z. Ye, X. Y. Wang, Y. X. Xu , and J. Feng, "Static and kinematic behaviour of a foldable truss roof structure", Advanced Steel Construction, 14(4), 14, 2017.
[15] V. S. Rajashekhar, K. Thiruppathi, and R. Senthil, "Modelling, Simulation and Control of a Foldable Stair Mechanism with a Linear Actuation Technique", Procedia Engineering, 97, 1312-1321, 2014.
[16] C. J. Gantes, *Deployable structures: analysis and design*. Boston: WIT Press, 2001.
[17] P. Fernández-Serrano, "Martino.:“The ‘movable Theatre’from Emilio Pérez Piñero. A Space-time Journey.”", Proceeding of the II National Congress of Pioneros de la arquitectura moderna Española: aprender de una Obra. Foundation Alejandro de la Sota, 2, 469-479, 2015.
[18] F. Escrig, J. Perez Valcarcel, and J. Sanchez, "Deployable cover on a swimming pool in Seville", Journal of the International Association for Shell and Spatial Structures, 37(1), 39-70, 1996.
[19] N. F. Dinevari, Y. Shahbazi, and F. Maden, "Geometric and analytical design of angulated scissor structures", Mechanism and Machine Theory, 164, 104402, 2021.
[20] K. K. Vu, J. Y. R. Liew, and K. Anandasivam, "Deployable Tension-Strut Structures: Structural Morphology Study and Alternative Form Creations", International Journal of Space Structures, 21(3), 149-164, 2006.
[21] F. Escrig, "Expandable space structures", International Journal of Space Structures, 1(2), 79-91, 1985.
[22] A. Kaveh and A. Davaran, "Analysis of pantographic foldable structures", Computers & Structures, 59(1), 131-141, 1996.
[23] W. Shan, "Computer analysis of foldable structures", Computers & Structures, 42(6), 903-912, 1992.
[24] T. Kokawa, "A trial of expandable arch," in *Proc. of IASS Symposium in Milano*, 1995, vol. 1, pp. 501-510.
[25] B. Willems, W. Dewulf, and J. R. Duflou, "Active snap-fit development using topology optimization", International Journal of Production Research, 45(18-19), 4163-4187, 2007.
[26] J. Pérez-Valcárcel, M. Muñoz-Vidal, F. Suárez-Riestra, I. R. López-César, and M. J. Freire-Tellado, "Deployable cylindrical vaults with reciprocal linkages for emergency buildings", Structures, 33, 4461-4474, 2021.
[27] J. Ma and T. Welo, "Analytical springback assessment in flexible stretch bending of complex shapes", International Journal of Machine Tools and Manufacture, 160, 103653, 2021.
[28] J. Muñoz, G. Jelenić, and M. A. Crisfield, "Master–slave approach for the modelling of joints with dependent degrees of freedom in flexible mechanisms", Communications in Numerical Methods in Engineering, 19(9), 689-702, 2003.
[29] DOSM, "Malaysia National Annex To Eurocode 3: Design of Steel Structures - Part 1-1: General Rules and Rules For Buildings", 2010.